

Chandra observations of Abell 2199

R. M. Johnstone*, S. W. Allen, A. C. Fabian and J. S. Sanders

Institute of Astronomy, University of Cambridge, Madingley Road, Cambridge CB3 0HA

Received

ABSTRACT

We present results from an analysis of two *Chandra* observations of the rich, nearby galaxy cluster Abell 2199. We find evidence (having corrected for projection effects) for radial gradients in temperature and metallicity in the X-ray emitting gas: the temperature drops from $kT \sim 4.2$ keV at $R=200$ kpc to 1.6 keV within $R=5$ kpc of the centre. The metallicity rises from ~ 0.3 solar at $R=200$ kpc to ~ 0.7 solar at $R=30$ kpc before dropping to 0.3 solar within the central 5 kpc. We find evidence for structure in the surface brightness distribution associated with the central radio source 3C338. No evidence is found for the gas having a large spread in temperature at any particular location despite the cooling time being short ($< 10^9$ yr) within the central ~ 15 kpc. Heating and mass cooling rates are calculated for various assumptions about the state of the gas.

Key words: galaxies: clusters: general – galaxies: clusters: individual: Abell 2199 – cooling flows – intergalactic medium – X-rays: galaxies

1 INTRODUCTION

Abell 2199 is a nearby rich cluster of galaxies, the central dominant galaxy of which is the cD galaxy, NGC 6166. The intracluster gas is of intermediate temperature (4.7 keV; Edge & Stewart 1991) and gives rise to X-ray emission which is strongly peaked on the central galaxy, leading to the suggestion of a strong cluster cooling flow, e.g., Peres et al. (1998).

NGC 6166 hosts the radio source 3C338 which has been known for nearly 20 years to have a peculiar morphology (Burns, Schwendeman & White 1983). Ge & Owen (1994) have shown that the radio emission from 3C338 suffers considerable depolarization and Faraday rotation which is consistent with the presence of a dense intracluster medium. Owen & Eilek (1998) have compared the ROSAT HRI X-ray image with a 5GHz radio map and found evidence for a strong interaction between the radio source and the X-ray emitting gas (with the X-ray gas disrupting the radio source). They argue that the intracluster medium is being heated by the radio source.

2 OBSERVATIONS

Two observations of Abell 2199 were made using the Advanced CCD Imaging Spectrometer (ACIS-S) on the *Chandra* satellite. Details are given in Table 1. The standard reprocessed level-two events files have been used for analysis

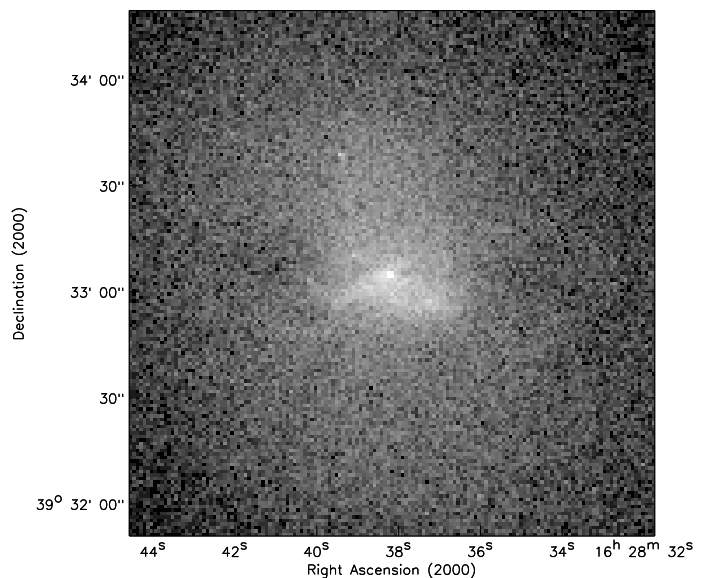


Figure 1. Raw X-ray image in the 0.3–7.0keV band. The data have been binned to 1 arcsec bins.

after screening for background flares. Throughout, we adopt a redshift for Abell 2199 of $z = 0.0309$ and a cosmology with $H_0 = 50 \text{ km s}^{-1} \text{ Mpc}^{-1}$ and $q_0 = 0.5$, giving an angular diameter distance of 176 Mpc and a luminosity distance of 187 Mpc. The linear scale is 850pc per arcsec.

* E-mail: rmj@ast.cam.ac.uk

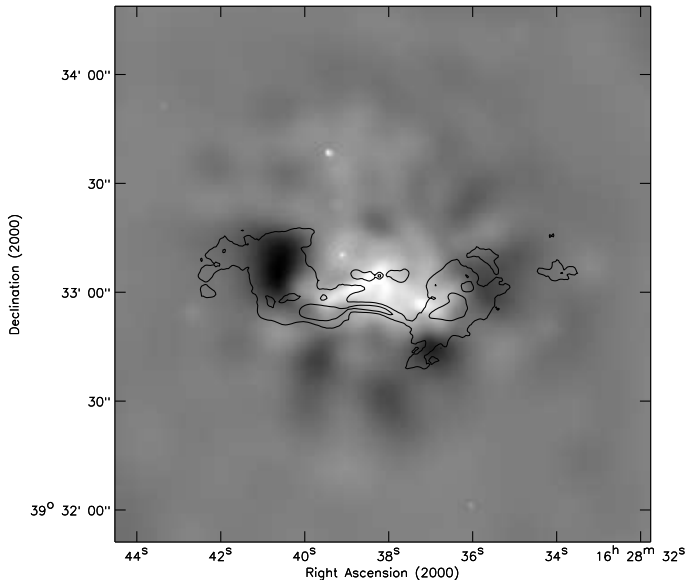


Figure 2. Contours from a 1.7 GHz radio map (Giovannini et al. 1998) overlaid on a difference image made from the X-ray data. The difference image is constructed by subtracting an image smoothed with a gaussian of standard deviation of 20 arcsec from the data which has been adaptively smoothed using a three sigma threshold. Surface brightness deviations can be seen at 20-40 arcsec from the nucleus to the east, south and west. The eastern radio lobe coincides with the eastern depression in surface brightness.

Date	Obsid	Seq num	FP Temperature (°C)	Duration (seconds)
2000 May 13	497	800005	-120	17319
1999 Dec 11	498	800006	-110	15771

Table 1. Log of observations. The columns show the observation date, observation identification number, observation sequence number, focal plane temperature and exposure time after the observation had been cleaned of background flare events.

In Fig. 1 we show the *Chandra* X-ray image of the central ~ 1 arcmin radius region of Abell 2199 in the 0.3-7.0 keV band. Events from both observations have been combined, taking into account the different aspect solution of the two data sets. The X-ray image was binned to have 1 arcsec pixels. A faint X-ray point source coincident with the active nucleus of NGC 6166 is seen at RA=16:28:38.24, Dec=39:33:04.3 (we use equinox 2000.0 coordinates thoughout). This has been the subject of a previous paper (Di Matteo et al 2001).

In Fig. 2 we show, as the image, the result of adaptively smoothing (using a three-sigma threshold) the X-ray data and then subtracting the gaussian smoothed (with standard deviation 20 arcsec) data. This emphasises deviations from the large-scale structure. Overlaid on this image is the 1.7 GHz radio map of 3C338 (Giovannini et al. 1998). Depressions in X-ray surface brightness are seen to the east,

south and west of the galaxy nucleus. There is a clear correspondence between the position of the eastern radio lobe and a marked depression in the X-ray surface brightness. The south eastern and north western ends of the western radio lobe are also associated with depressions in X-ray surface brightness.

For the case of the eastern radio lobe it may be that the radio-emitting plasma displaces the hot gas as is seen in the Perseus (Fabian et al. 2000) and other clusters (e.g. McNamara et al. 2000). The other depressions to the south may indicate the positions of older radio lobes.

The X-ray data do not account simply for the fact that the radio ridge which joins the two radio lobes is displaced to the south of the nucleus. It is plausible that motion of the nucleus is responsible for this, as discussed by Burns, Schwendeman & White (1983). Probably, it is not the nucleus alone which moves but much of the whole central galaxy and innermost cluster core. If, as seen in projection from Earth, the galaxy has oscillated, or orbited, to the south a distance of about 10 to 20 arcsec (8.5-17 kpc) and has now returned to the north with the radio source off for most of the return trip, then the radio structure may be explained. The bright X-ray emitting region which extends to the south of the nucleus could be a cooling wake, similar to that seen in Abell 1795 (Fabian et al. 2001a).

3 SPATIALLY RESOLVED SPECTROSCOPY

3.1 Analysis of data in projection

The two observations of Abell 2199 were taken with the focal plane at different temperatures, making it inappropriate to combine the event data directly for spectral analysis. We have therefore produced separate spectral files, response data and background files for the two observations, and fitted models to the two observations simultaneously using XSPEC (Arnaud 1996). Response matrices and effective area files were made by averaging a 32×32 grid of calibrations covering chip 7, using the CIAO tools MKRMF and MKARF, and using weighting factors equal to the number of counts (in the 0.5-7.0 keV band) in the source in the region covered by the calibration. Background spectra were generated from corresponding regions of the standard background fields using software and data from Maxim Markevitch at http://asc.harvard.edu/cal/Links/Acis/acis/Cal_prods/bkgrnd/current/index.html.

Initially we did not wish to impose a particular geometry on the possible spatial variation of spectral parameters. Therefore, we have used a technique based on the adaptive binning algorithm of Sanders & Fabian (2001) to define tiled square regions of the image where there are at least 1000 counts by progressively increasing the binning of a spatial map until that threshold of counts is reached. Pulse invariant spectra were then extracted from these regions and fitted over the nominal 0.5-8.0 keV band with single temperature MEKAL (Kaastra & Mewe 1993; Liedahl et al. 1995) plasma emission models that were allowed to have a freely fitting value for the foreground absorption. (Discrete point sources visible in the *Chandra* image at positions listed in Table 2 have been excluded from the analysis). We present the results of these fits in Fig. 3.

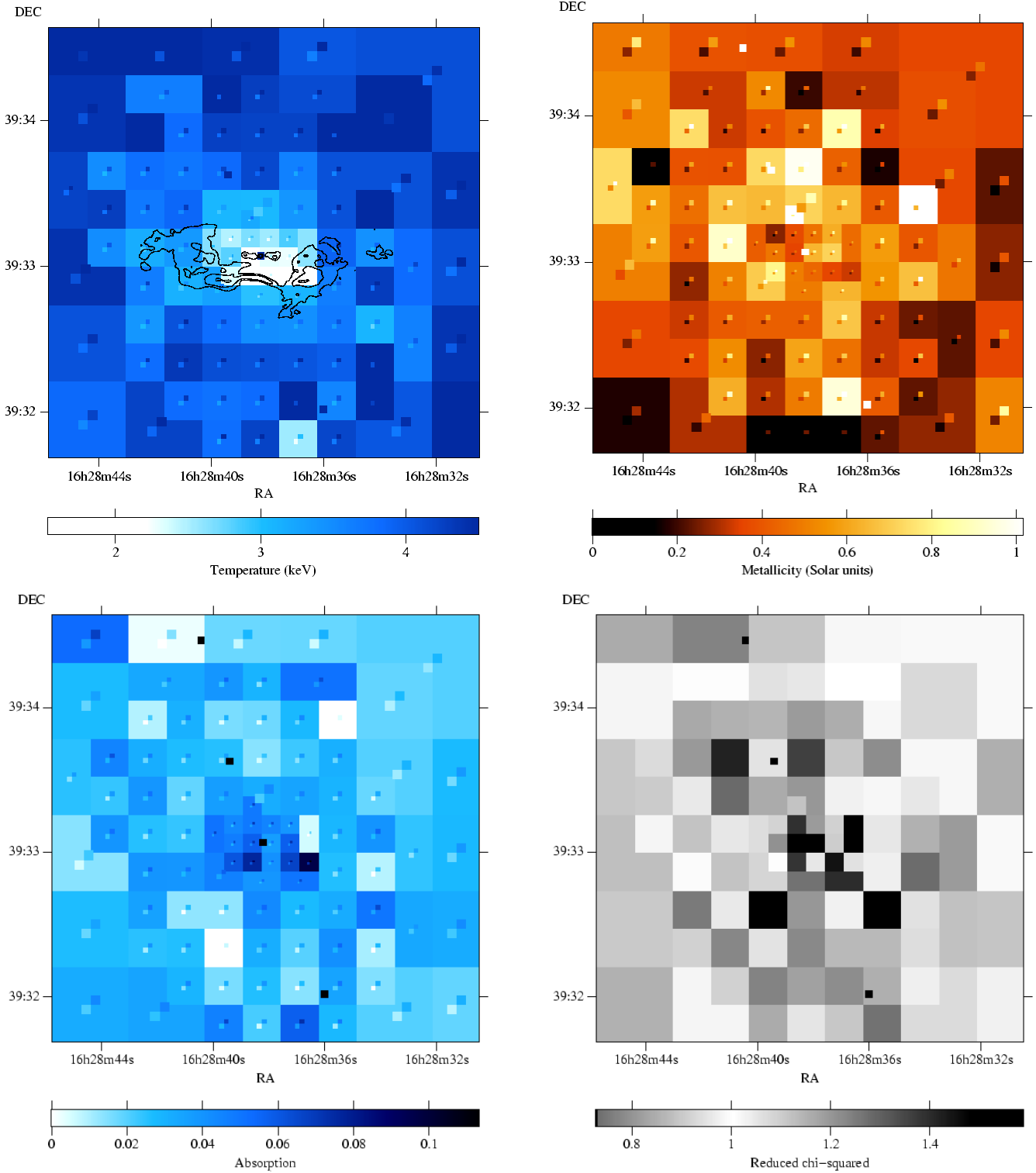


Figure 3. Temperature (with radio contours overlaid) (upper left), metallicity (upper right), absorption (in units of $\times 10^{22} \text{ cm}^{-2}$) (lower left) and reduced chi-squared (lower right) maps of Abell 2199 determined from spectral fitting of data extracted from adaptively binned spatial regions. The small dot pairs inside each bin show the 1σ uncertainty on the values. Regions excluded from the analysis due to the presence of a point source are marked as small black or white squares.

RA (Equinox 2000)	Dec
16:28:26.2	39:33:53
16:28:38.3	39:33:04
16:28:39.2	39:33:10
16:28:39.5	39:33:38
16:28:40.5	39:34:28

Table 2. Positions of point sources excluded from analysis.

The temperature map shows significant variations between adjacent pixels. There is a trend in that the temperature drops from values of 4–4.5 keV around the outside edge of our map ($R \sim 75$ kpc) to values between 1.6–2.2 keV near the nuclear point source. The significance of pixel-to-pixel variations in the metallicity map is much less marked at the edge of our region (where values are between 0.15–0.3 of the solar value), due to the much larger percentage error on this quantity. However, within the inner 45 kpc of the cluster there are significant variations, with individual pixel metallicities varying between 0.25 and 1.2 times the solar value. The absorption map shows that the equivalent neutral hydrogen column density is at least $2 \times 10^{20} \text{ cm}^{-2}$ over most of the mapped region. Only a few pixels are consistent with the value expected from our Galaxy for which $N_H = 8.7 \pm 0.6 \times 10^{19} \text{ cm}^{-2}$ (unweighted average of surrounding grid points; Dickey & Lockman 1990) in the direction of Abell 2199. Near the centre of the cluster the absorption rises to between $5 - 10 \times 10^{20} \text{ cm}^{-2}$. Finally the map of reduced chi-square shows that most of the pixels have values of chi-square between 0.8 and 1.2. Only a few pixels, predominantly near the centre of the cluster have higher values.

We have overlaid the radio contour map on the temperature map, to facilitate comparison. Although no detailed correlation is evident between structure in the temperature or metallicity maps and the radio map, the cooler regions of the cluster are associated with the radio brighter parts of the radio source.

In Fig 4 we have plotted the values of absorption column density, temperature and metallicity as a function of the radial distance of the bin from the cluster centre. Inspection of this plot confirms that most bins at similar radii have similar properties although there are a small number of values inconsistent with the mean for that radius. In particular, we have looked at the region near the two cool pixels centred on (RA=16:28:36.9, Dec=39:32:55.8). We find that a single temperature fit gives $kT \sim 1.3$ keV, rather cooler than the surrounding regions.

3.1.1 Single temperature radially varying models

In the absence of evidence for gross non-radial variations in the properties of the gas we have made spectra binned azimuthally into eight concentric rings out to a radial distance of 200 kpc from the central point source. One further irregular shaped bin is included which contains all of the data that are outside 200 kpc radius region but which still lie on chip 7. Bins beyond a radial distance of 140 kpc from the nucleus cover slightly different spatial regions in the two data

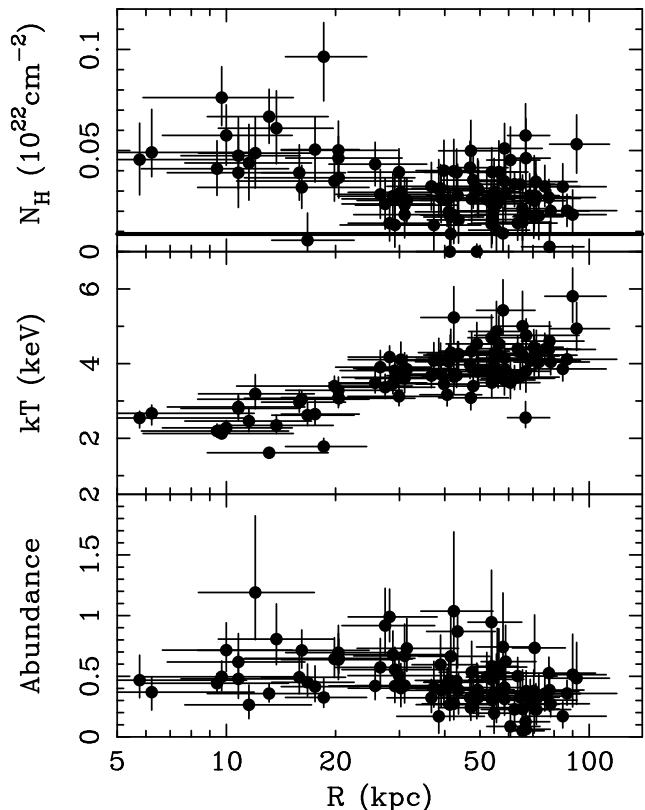


Figure 4. Radial variation of absorption, temperature, metallicity in Abell 2199 as measured from a single temperature model fitted to the adaptively sized bins. The solid line in the absorption panel shows the Galactic value of the neutral hydrogen column density.

sets, because the cluster is not centred on the chip and the spacecraft roll angle was different for the two observations.

We have fitted a single temperature MEKAL model absorbed by a foreground screen (to account for absorption from the Galaxy) to each of the concentric spatial regions. Fig. 5 shows the radial profiles of temperature, metallicity, equivalent hydrogen absorbing column density and reduced chi-square. The absorption, parameterised as the equivalent column density of neutral hydrogen, is greater than that expected from 21cm observations of the Galaxy throughout the region studied. (This may be related to uncertainties in the calibration of the instrumental effective area below 1keV¹). Even with this caveat, though, we see an increase in the absorption within the central 20 kpc, relative to that seen further out, by $\sim 2 \times 10^{20} \text{ cm}^{-2}$.

The cluster shows a smoothly declining temperature profile that starts at ~ 4.2 keV beyond 200 kpc, reducing to near 2 keV within the central 5 kpc. The broad-beam temperature for this cluster was measured with EXOSAT as 4.7 ± 0.4 keV by Edge & Stewart (1991) indicating that the temperature profile climbs further beyond the spatial extent of our analysis. Our outer measured temperature is in good agreement with the value of 4.16 ± 0.15 keV measured from the central 4-5 arcmin radius region by ASCA (Allen et al. 2001a).

¹ http://cxc.harvard.edu/cal/Links/Acis/acis/Cal_projects/index.html

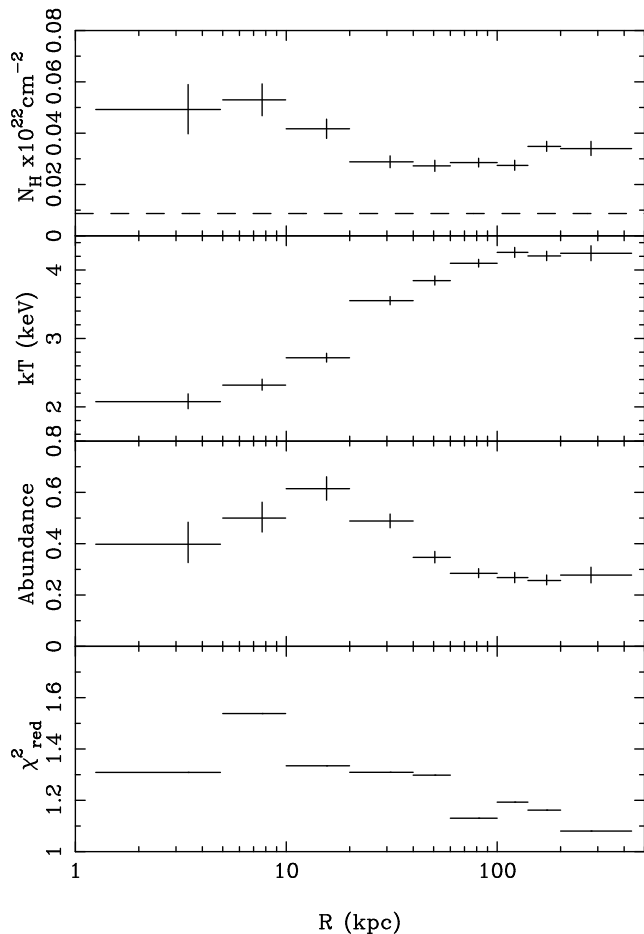


Figure 5. Radial variation of absorption, temperature, metallicity and reduced chi-square in Abell 2199. The dashed line in the absorption panel shows the Galactic value of the neutral hydrogen column density.

Within the central 5kpc we find that the metallicity is close to the ASCA measured value for the central 4-5 arcmin radius region (Allen et al. 2001a) of 0.4 times the solar value. (We use the default solar abundance set given by Anders & Grevesse 1989). By a radial distance of 15kpc, the metallicity has risen to 0.6 times the solar value, before reducing again at larger radii to near 0.25 times the solar value.

3.1.2 Multi-temperature models

We have also examined the annular spectra using multi-temperature models. We first fitted the data with a two-temperature model consisting of freely fitting absorption acting on two single-temperature emission components; the abundances were tied together but the temperatures were allowed to fit freely. The introduction of the second emission component is required (at the 99 per cent confidence level, determined using an F-test) for the three radial bins 10–20kpc, 20–40kpc and 140–200kpc. However, in section 3.2.1 we show that the evidence for multi-temperature components in these annular regions is largely due to projection effects.

Recently, Protassov et al. (2002) have questioned the validity of using the F-test to test for the significance of an

additional additive component when fitting models to data because the hypothesis is on the boundary of the parameter space. In our case we have used the F-test to check whether a second MEKAL component is statistically required by the data. This is on the boundary of parameter space since the null hypothesis is that the second MEKAL component is not required. In this case the normalization of the second component is zero, and negative normalizations (although possible in practice within the fitting code) are excluded from the fitting procedure as they are not physically meaningful. We have carried out fits to Monte Carlo realizations of our data and find that (in our case) the distribution function of our measured F values matches the formal F distribution very well for values of F above 0.2².

We next explored the effect of replacing the second temperature component with a cooling flow spectrum (in which gas cools to zero degrees from the plasma temperature). We obtain similar results to those found with the two-temperature model and place limits on the size of the cooling flow component within R=100kpc of $12 \pm 3 M_{\odot} \text{ yr}^{-1}$ or $37_{-13}^{+14} M_{\odot} \text{ yr}^{-1}$ (90 per cent confidence limits), depending whether or not freely fitting intrinsic absorption is included on the cooling flow component.

We have also investigated the region, mostly to the south of the nucleus, defined by the polygon with the following vertices: (16:28:40.03,39:32:54.7), (16:28:40.03,39:32:54.7), (16:28:38.17,39:33:12.9),

2

To check the validity of the F-test we have repeatedly run fits with single and two-temperature MEKAL models to Monte Carlo realizations of our data (generated using the XSPEC FAKEIT command) and looked at the distribution of the F-statistic. One thousand realizations of our data were generated from the single temperature plasma model (with freely fit absorption) which best fitted one combined data set, by folding the model through the detector response function and adding random noise appropriate to the total counts generated. First we fitted the same model that was used to generate the data and noted the chi-square value and number of degrees of freedom. We then fitted a two-temperature MEKAL plasma model in which the metallicity of the second component was fixed to that of the first and the absorption component acted on both MEKAL components. The temperature and normalization of the second component are then the new fit parameters; we logged the value of the chi-square statistic and number of degrees of freedom in this case.

A Kolmogorov-Smirnov test was used to determine whether the distribution of measured F values was significantly different from the true F distribution. For all values of F above 0.2 we find the two distributions to be in excellent agreement (the probability of differences between the two cumulative distribution functions as large as observed (if they are the same distribution) is greater than 20 per cent).

Below a measured F-value of 0.2 the two distributions are significantly different (much less than 1 per cent chance of deviations as large as observed if the two distributions are the same). This may be due to either to XSPEC sometimes not finding the exact minimum value of chi-square, or to problems with the test discussed by Protassov et al. (2002).

Since the critical values of F used in our assessment of the significance of extra spectral components in this paper lie near F=4.6, we conclude that the boundary condition problem does not affect our inferences.

(16:28:36.25,39:32:54.2), (16:28:40.05,39:32:54.1), but excluding a region of radius 2.5 arcsec centred on the nucleus. This region was targeted for separate analysis because it stands out as having a higher surface brightness than surrounding regions. We find that the gas temperature (fitted with a single-temperature model) is cool ($T = 2.5 \pm 0.1$ keV) and that the data can accommodate a cooling flow of up to $9 M_{\odot} \text{ yr}^{-1}$. Since this triangular region contains regions of bright radio emission we have checked for the presence of power-law continuum X-ray emission. No significant such emission was found: a two temperature fit is significantly better than a single temperature plus power-law continuum.

3.2 Analysis of data accounting for projection effects

3.2.1 Single temperature fits

Assuming that the cluster is spherically symmetric and that the physical conditions change only in the radial coordinate of the cluster, we can account for the projection effects of gas exterior to a particular region. This allows us to determine the physical conditions in the gas as a function of the true 3-dimensional radial coordinate. We do this by fitting spectra from concentric rings simultaneously using multiple MEKAL models. We allow one MEKAL model for the outermost annulus, two for the next one in and so on, setting the normalizations of the different projected components according to the relative volumes of the shells. The technique is described in full in Allen et al. (2001b). Another approach, used on the cluster Abell 1795, is described by Ettori et al. (2002).

The temperature and abundance profiles obtained from this method are shown in Fig. 6. The Galactic absorption was allowed to be a free parameter and its value was determined as $3.05 \pm 0.09 \times 10^{20} \text{ cm}^{-2}$. The temperature profile shows the central bin to be cooler than that measured in the projected data: $1.57^{+0.20}_{-0.16}$ keV compared with $2.08^{+0.12}_{-0.10}$ keV. The profiles both from the simple analysis presented in section 3.1.1 and from this analysis asymptote to similar values, $4.26 \pm 0.07 \text{ keV}$ (deprojected) and $4.21 \pm 0.07 \text{ keV}$ (seen in projection) at radii of 140-200kpc.

The deprojected abundance profile is very similar to that seen in the simple single-temperature fits to the data in projection. The low value seen in the central bin, and the value seen at the abundance maximum near 20 kpc, are more extreme in the deprojected analysis but with larger uncertainties.

3.2.2 Two temperature fits

Finally, we have investigated whether there is a statistical requirement for a second emission component in any annulus, once the projection of the first emission components have been taken into account. To do this, we use the XSPEC PROJCT model and add in second emission components to each annulus successively (starting at the outside, allowing only the temperature and normalizations to be freely fit), and note how the value of the chi-square statistic reduces. In each case the metal abundance of the second component is tied to the metal abundance of the corresponding first component, and a single absorption component is applied

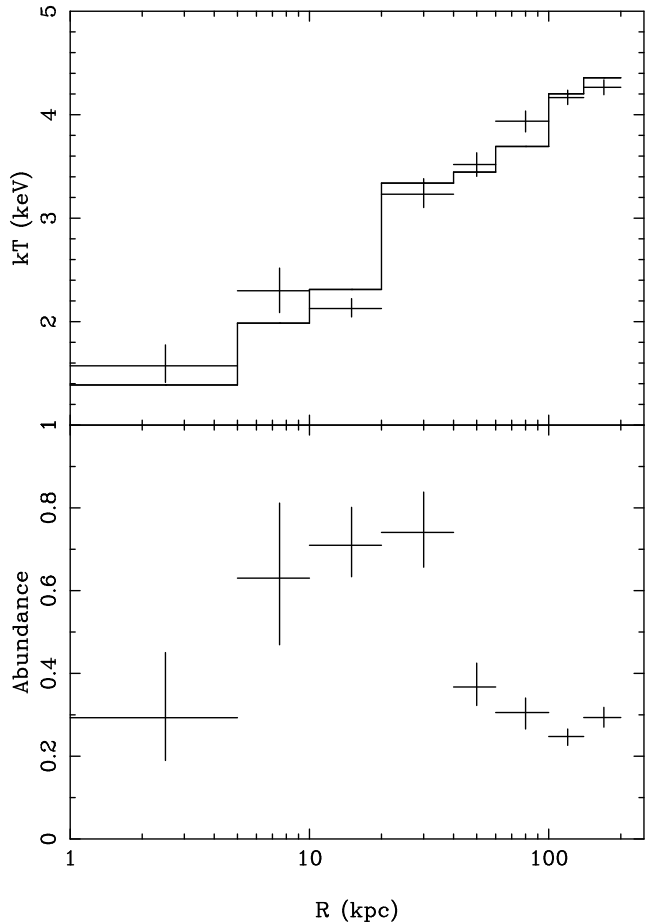


Figure 6. Intrinsic (3-dimensional) radial variation of temperature and metallicity in Abell 2199. The solid line plotted over the temperature profile is the Navarro et al. (1997) (NFW) profile which best fits the data.

to the whole model. The fiducial fit, in which each region has only one emission component, gave a value $\chi^2 = 4865.3$ for 3761 degrees of freedom. Table 3 shows the values of the chi-square statistic, number of degrees of freedom and corresponding values of the F-statistic, together with the formal probability that such a large value of F would be obtained if the new emission component was not required. We caution that due to the large value of the reduced chi-square statistic the true probabilities will be larger than listed in the table, so the results are less significant than tabulated.

We find that the outermost region strongly requires a second emission component. This is not surprising since by definition we have not accounted for the projection of emission external on to this region. There is also evidence, but at a lower significance, for a second emission component being required between 20-100kpc.

4 IMAGE DEPROJECTION AND MASS ANALYSIS

The deprojected temperature and surface brightness profiles can be used to constrain the mass profile of the cluster. For this analysis we have used the methods described by Allen et al. (2001b) and Schmidt, Allen & Fabian (2001). In

Region (kpc)	χ^2	DoF	F	F_{prob}
140-200	4833.0	3759	12.6	3.7E-6
100-140	4823.4	3757	3.7	2.4E-2
60-100	4802.7	3755	8.1	3.1E-4
40-60	4788.5	3753	5.6	3.9E-3
20-40	4770.5	3751	7.1	8.6E-4
10-20	4761.2	3749	3.6	2.6E-2
5-10	4755.3	3747	2.3	9.6E-2
0.8-5	4750.9	3745	1.7	1.8E-1

Table 3. Values of χ^2 , number of degrees of freedom, the F statistic and corresponding probability for including a second emission component in each region successively, starting from the outermost region.

NFW	Moore	NIS
$r_s = 130 \pm 10$ kpc	$r_s = 650^{+250}_{-150}$ kpc	$r_c = 20^{+1}_{-2}$ kpc
$c = 9.7 \pm 0.5$	$c = 2.6^{+0.5}_{-0.6}$	
$\sigma = 467 \pm 12$ km s $^{-1}$	$\sigma = 625^{+75}_{-70}$ km s $^{-1}$	$\sigma = 600 \pm 10$ km s $^{-1}$
$\chi^2 = 15.9/6\text{DoF}$	$\chi^2 = 23.7/6\text{DoF}$	$\chi^2 = 20.2/6\text{DoF}$

Table 4. Parameters obtained from fitting mass models to the temperature profile.

brief, the observed surface brightness profile and a particular parameterized mass model are together used to predict the temperature profile of the X-ray gas, which is then compared with the observed, spectrally-determined results.

Three separate parameterizations for the cluster mass distribution were examined: the Navarro et al. (1997) (NFW) profile, the Moore et al. (1998) profile and a non-singular isothermal sphere (NIS). We find that the NFW profile provides (marginally) the best fit to the data, although all three models give formally unacceptable results. Table 4 lists the best-fit parameters for the three models, together with their 1σ uncertainties, chi-square values, and the number of degrees of freedom for the fit. For the NFW and Moore profiles we note that there are only two fit parameters; the scale radius, r_s , and the concentration parameter, c . However, we also quote values for the effective velocity dispersion $\sigma = \sqrt{50}r_s c H$, which is a function of the other two variables and the Hubble constant.

The temperature profile predicted by the best-fit NFW mass model overplotted on the observed, deprojected temperature profile is shown in the top panel of Fig. 6. The total gravitating mass profile associated with the best-fit NFW model is plotted in Fig. 7, along with its 1σ uncertainties.

The shape of the inner gravitational well around NGC6166 has been probed by the optical spectroscopy of Carter, Bridges & Hau (1999), who find that the velocity dispersion of the galaxy rises outward. Recently Kelson et al. (2002) have confirmed and extended this result. They found that the velocity dispersion continues to rise out to the limit of their data at 60kpc, by which time the stellar velocity dispersion is close to that of the cluster galaxies. Kelson et al. (2002) note that our measurement of the mass within

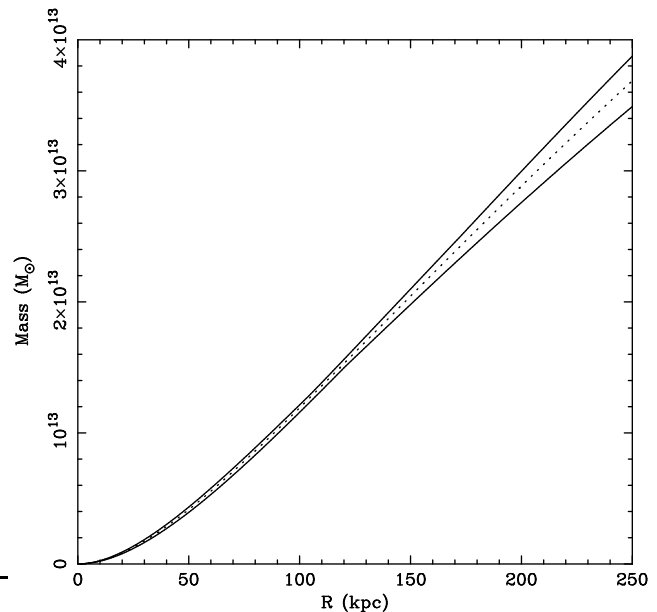


Figure 7. Mass profile (dotted line) of the core of Abell 2199 determined from the NFW potential which best fits the temperature profile. The solid lines show the 1σ uncertainty limits.

$0.1h^{-1}\text{Mpc}$ (where $h = H_0/100$) is in reasonable agreement with their determination, for the same region.

We next used the best-fitting gravitational potential that was determined above to constrain an image deprojection analysis of the Abell 2199 cluster. We follow the method of Fabian et al. (1981) in determining the physical conditions in the cluster as a function of the radius. The Galactic value of the column density is used. Error bars for the derived quantities were determined from one hundred Monte Carlo replications of the original data.

In Fig. 8 we show the major results from the deprojection analysis. The input surface brightness distribution is shown in the top panel together with the implied electron density, cooling time and mass deposition rate in lower panels.

The nominal mass deposition rate integrated out to the point where the cooling time is equal to the age of the universe is $150 M_\odot \text{ yr}^{-1}$. However, the spectral fits (section 3.1.2) place a limit on the mass deposition rate of less than $\sim 50 M_\odot \text{ yr}^{-1}$ suggesting that any steady state cooling flow must be younger than 2–3 Gyr (associating the age of the cooling flow with the cooling time of gas where the mass deposition rate from the image deprojection equals that in the spectral fits).

5 HEATING AND COOLING RATES

We have seen that the radiative cooling time of the gas in Abell 2199 is less than about 7 Gyr within a radius of 100 kpc, less than 2 Gyr within 20 kpc and about 0.1 Gyr within the innermost few kpc. The temperature decreases from above 4 keV beyond 100 kpc to 1.6 keV (deprojected) within 5 kpc. This overall appearance suggests that a cooling flow may be operating (see e.g. Fabian 1994), but the spectral analysis provides only modest support and then

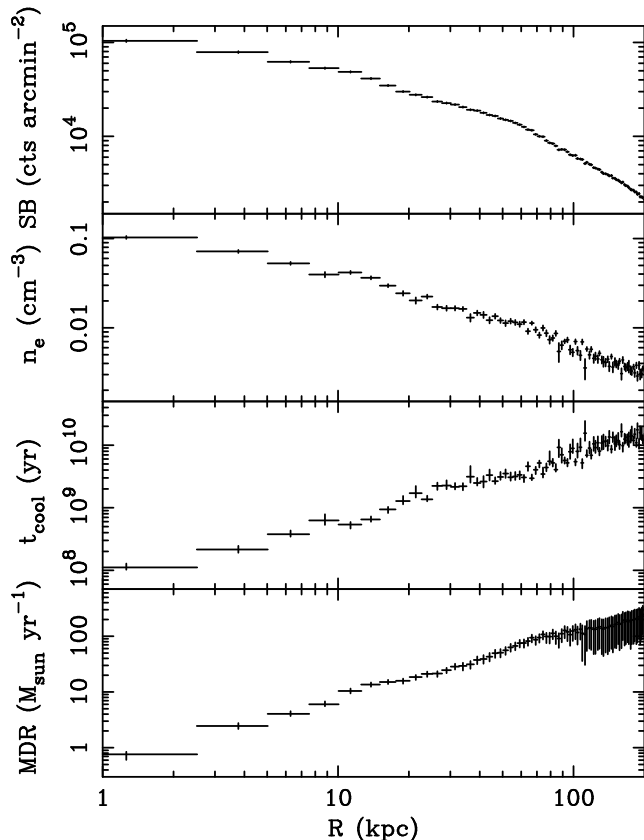


Figure 8. Image deprojection results of Abell 2199. The top panel shows the input surface brightness profile, while the lower three panels show the derived electron density, cooling time and mass deposition rate profiles in the cooling flow.

only for a small flow of tens $M_{\odot} \text{ yr}^{-1}$. XMM-Newton Reflection Grating Spectrometer (RGS) data of other clusters also show little evidence for long-lived, steady-state cooling flows, in which gas cools from the cluster virial temperature to below 10^6 K by emitting observed X-radiation (Peterson et al. 2001; Tamura et al. 2001; Kaastra et al. 2001). The RGS spectra, which do not spatially resolve any flow, are consistent with the gas cooling from the virial temperature to about one third to one fifth of that value but no lower, possibly in a single-phase cooling flow. The fate of the coolest gas, at 1–2 keV, is unknown. It may be heated, mixed with much cooler gas or expelled (see e.g. Fabian et al. 2001b).

Here we attempt to quantify upper limits to the amount of multiphase gas in the core of Abell 2199, and to see where the steady-state cooling flow assumption breaks down. Using a similar (PROJCT) spectral model, accounting for the projection of outer components on to inner regions, to that discussed in section 3.2.2, limits on the volume filling fraction (f_2) of any second emission component in the central four spatial bins (out to 40 kpc from the centre of the cluster) were calculated using

$$f_2 = \left[1 + \frac{e_1}{e_2} \left(\frac{T_1}{T_2} \right)^2 \right]^{-1}, \quad (1)$$

Sanders & Fabian (2002). e_1 and T_1 are the emission measure and temperature of the first temperature component

for a particular shell, and e_2 and T_2 are the emission measure and temperature of the additional component. Unlike section 3.2.2 we only applied the second emission component to one spatial region at a time. The second component has a freely fitting normalization and a metal abundance that is fixed to the metal abundance of the first component. We stepped the temperature of the second component through a range of values from 0.5 keV to 2.5 keV, calculating f and its uncertainty σ_f (obtained by propagating the uncertainties in e_1 , e_2 , and T_1). Where the value of f is less than $3\sigma_f$ we plot an upper limit at $3\sigma_f$. Our results are shown in Fig. 9. Also shown, in Fig. 10, for comparison, is the continuous differential filling factor distribution expected from a constant pressure cooling flow.

It is clear that there is little evidence for the gas being multiphase at any radius. (Note that the ‘detections’ of a second component at some temperatures in the 10–20 kpc region may be in large part due to the projection of the second component present in the 20–40 kpc region). For a continuous distribution of temperatures the y-axis is df/dT (Fig. 10) and limiting curves lie below the plotted temperature limits which represent the step by step values for one additional temperature component only. (Note also that the test applied in section 3.2.2 is different from the test applied here, as in the former each additional component added to outer rings was left in when evaluating the F-statistic for the interior ring, whereas here we have added the second component in for each region separately and then removed it before adding in the second component for the next region).

Since the temperature distribution appears to be close to single phase, we have then tested whether it resembles a single-phase cooling flow dropping to some minimum temperature $T_{\text{min}} \sim 1$ keV. Although the temperature profile (Fig. 6) appears consistent with a single-phase cooling flow, the surface brightness profile is not. This is the reason that multiphase flows were introduced in the first place (e.g. Fabian, Nulsen & Canizares 1984). Fig. 11 (solid points) shows the distribution of emission measure against radius. We use the normalizations from XSPEC, which need to be multiplied by $3.8 \times 10^{68} \text{ cm}^2$ to convert to cm^{-3} .

Also plotted is the distribution expected from a single phase cooling flow of $100 M_{\odot} \text{ yr}^{-1}$, both with and without the gravitational work done included. To obtain this we use the energy equation of a steady state spherical inflow,

$$-\dot{M} \int \left(\frac{5}{2} \frac{k}{\mu m} \frac{dT}{dr} + \frac{d\phi}{dr} \right) dr = -e\Lambda + h. \quad (2)$$

μm is the mean mass per particle, h the heating rate (assumed zero for Fig. 11), e the emission measure and ϕ the gravitational potential, obtained from Fig. 7.

We see that the observed emission measure distribution is nowhere as flat as expected from a single-phase flow (the expected values scale up and down with \dot{M}). There is too little emission at small radii and too much at large radii. The latter can be explained by any flow not yet having reached a steady-state, but the lack of emission at the centre is more difficult to understand. We have already shown that spectral fits to the data exclude any simple distributed mass dropout such as expected from a multiphase flow with a mass deposition rate greater than $15 M_{\odot} \text{ yr}^{-1}$. However, a flow can be accommodated if the gas, or its emission, can be made to be unobservable. Including absorption is one way to achieve

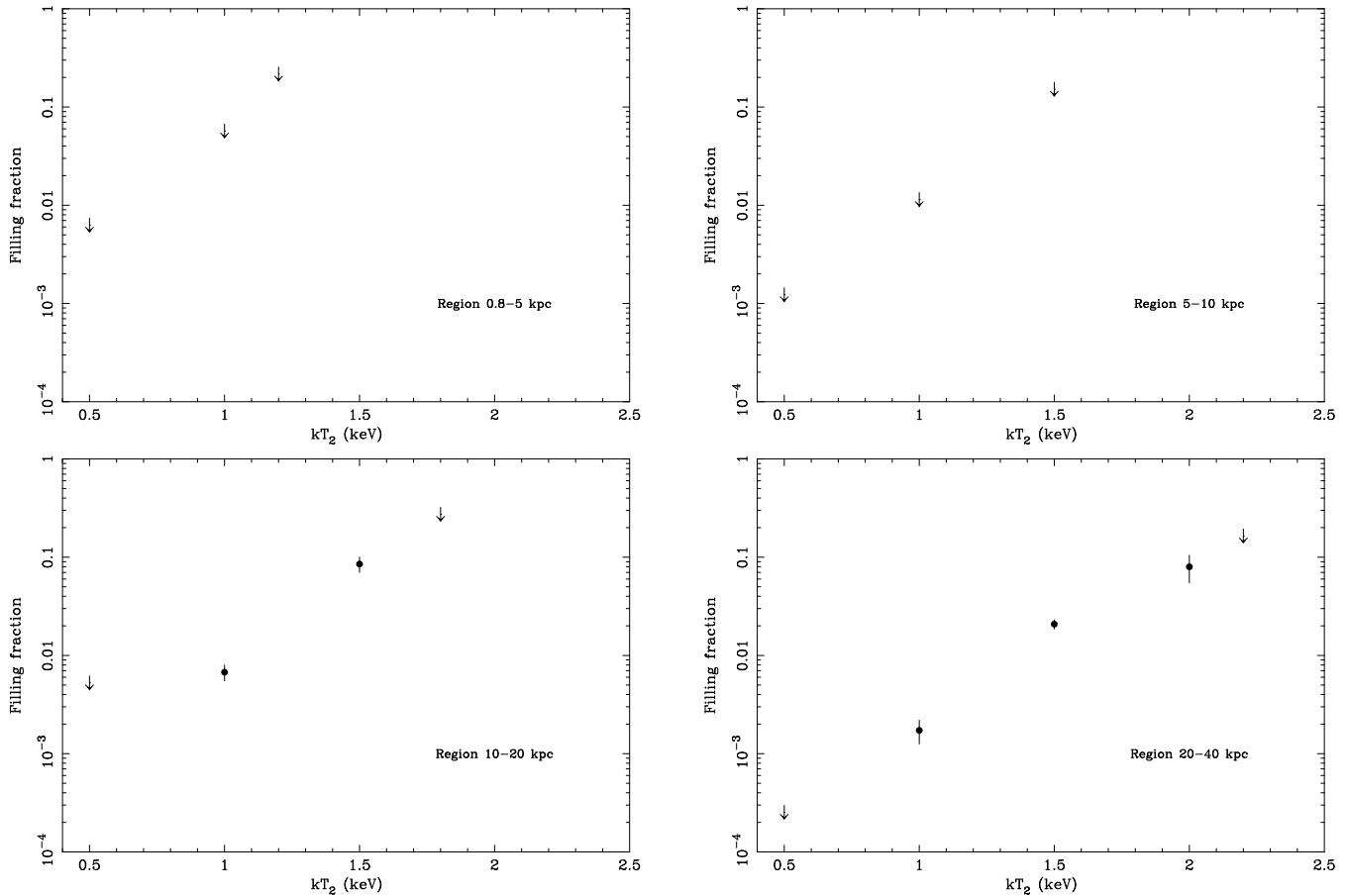


Figure 9. Volume filling fractions of a second temperature component, in the innermost four spatial regions, as a function of temperature.

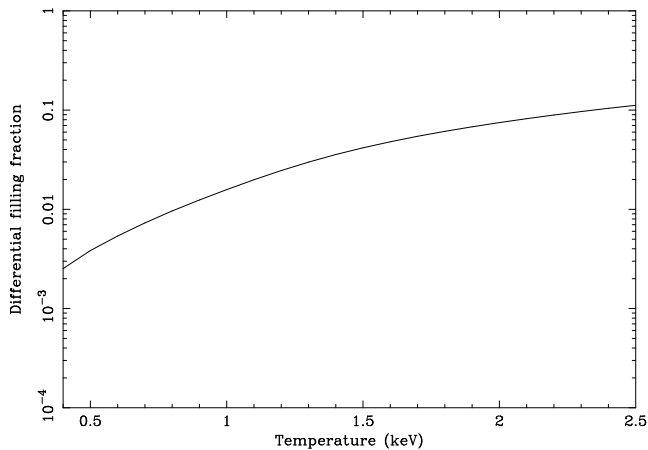


Figure 10. Differential filling fraction distribution of gas cooling from 2.5keV at constant pressure

this, and the spectral data allow up to $\sim 50 M_{\odot} \text{ yr}^{-1}$ if the emission is absorbed. The missing soft X-ray luminosity in cooling flows is discussed more extensively by Fabian et al. (2002).

Finally, we have quantified the heating required to maintain the gas in a steady state (Fig. 12), by estimating h from equation (2). Here a negative value for the heating means that heat has been lost in a non-radiative manner

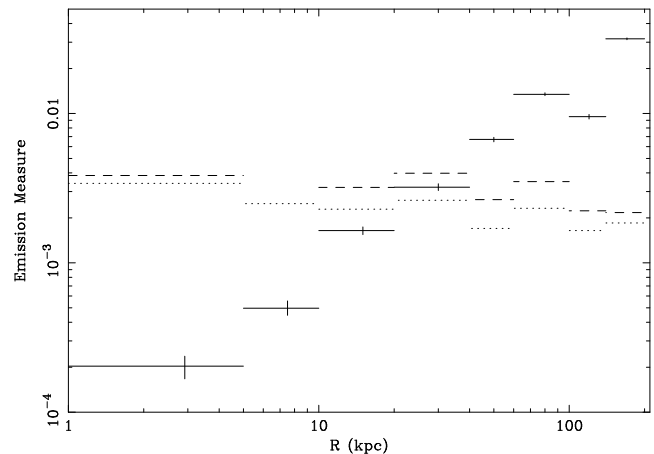


Figure 11. The emission measure (in XSPEC units) of gas in each annulus, determined from the deprojected spectral fitting procedure (solid points). The dashed curve shows the emission measure distribution expected from single-phase gas cooling in the inferred gravitational potential at a rate of $100 M_{\odot} \text{ yr}^{-1}$. For comparison the dotted curve shows the result for an isobaric, single-phase flow.

(for example by mixing with cold gas). *Heating must be distributed over a wide range of radii*, with a heating rate per unit volume proportional to $r^{-1.5}$ if there is no mass dropout. The results are only relevant where some steady-state can be

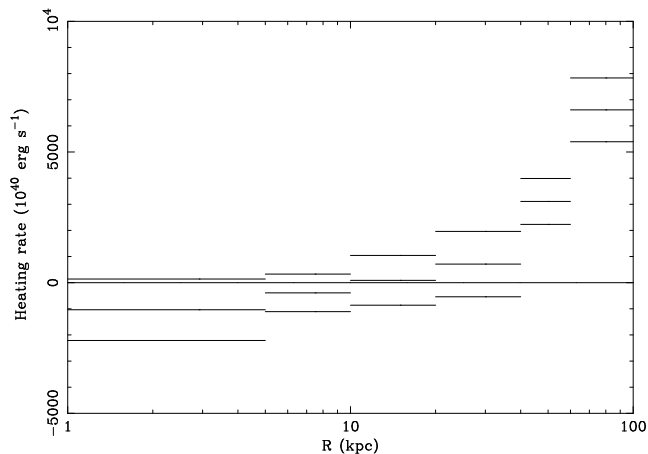


Figure 12. The heating rate required to maintain thermal equilibrium for a single phase inflow of 0 (upper lines), 50 (middle lines) and $100 M_{\odot} \text{ yr}^{-1}$ (lower lines).

assumed. Note that the radio source, at present, affects the gas distribution in the east-west axis out to about 30 kpc.

The peaked abundance distribution determined from the deprojected spectral analysis, Fig. 6, argues against much mixing, or convection of gas across the annulus at 20–30 kpc. The whole of the current gas distribution is stable against convection since the entropy, $S \propto T/n^{2/3}$, monotonically increases with radius ($S \propto r^{0.8}$ from a few kpc to about 100 kpc since the deprojected gas temperature is approximately $1.11r^{0.29}$ keV and the electron density is $0.21r^{-0.75} \text{ cm}^{-3}$, where the radius r is in kpc).

6 CONCLUSION

The core of Abell 2199 is complex. Some depressions in the X-ray surface brightness are seen to coincide with the radio lobes. Other depressions to the south may indicate earlier radio activity. The temperature decreases from 4.2 keV to 1.6 keV over radii from 100 kpc to 5 kpc, which is where the radiative cooling time drops from 7 Gyr to 0.1 Gyr. The X-ray surface brightness is not sufficiently peaked however to be consistent with a single phase cooling flow. We find no strong evidence for multiphase gas in the cluster core except in the 20–40kpc region where the radio lobes have disturbed the gas most. We limit the mass deposition rate within the central 100 kpc to $12 M_{\odot} \text{ yr}^{-1}$. Only if the emission below about 1 keV is somehow undetectable, such as occurs if there is intrinsic absorption, can this rate be significantly increased to around $40 M_{\odot} \text{ yr}^{-1}$.

We have quantified the heating rate and its distribution in the cluster required to balance cooling if the gas is in a steady state. However, the situation may not be steady. Any cooling flow is only likely to occur and have become steady within the region where the cooling time is a few billion year or less. The radio source is clearly causing disruption to the south, east and west of the nucleus. How much disruption is perhaps indicated by the abundance profile. Our spectral fitting shows that the evidence for two temperatures is almost entirely due to projection effects and Fig. 6 gives the best description of the state of the gas. The abundance shows a maximum at around 30 kpc. The profile (which

has a similar shape to that seen in the Centaurus Cluster; Sanders & Fabian 2002) is consistent with some mixing of gas within, but not much beyond, that radius. Abundance gradients can be due to metal injection by SN Ia in the central galaxy (Dupke & White 2000; Ettori et al. 2002) and are expected to show a monotonic increase inward (unless the metals are poorly mixed and cooling dominates; Morris & Fabian 2002, in preparation). A central decrease can be explained by some exchange of gas between the centre and the region at 40–50 kpc (or further out). Why intermediate radii have not been similarly affected is puzzling. Massive mixing should however have wiped out the gradient. The high abundance of the gas at 10–40 kpc indicates that it has probably resided close to the centre of the galaxy for an extended period.

ACKNOWLEDGMENTS

We thank Stefano Ettori for the use of his software to make exposure maps and to extract surface brightness profiles. SWA and ACF acknowledge support by the Royal Society.

REFERENCES

- Allen S.W., Fabian A.C., Johnstone R.M., Arnaud K.A., Nulsen P.E.J., 2001a, MNRAS, 322, 589
- Allen S.W., Ettori S., Fabian A.C., 2001b, MNRAS, 324, 877
- Anders E., Grevesse N., 1989, *Geochimica et Cosmochimica Acta*, 53, 197
- Arnaud K.A., 1996, *Astronomical Data Analysis Software and Systems V*, eds. Jacoby G. and Barnes J., p17, ASP Conf. Series volume 101
- Burns J.O., Schwendeman E., White R.A., 1983, ApJ, 271, 575
- Carter D., Bridges T.J., Hau G.K.T., 1999, MNRAS, 307, 131
- Dickey J.M., Lockman F.J., 1990, ARAA, 28, 215
- Di Matteo T., Johnstone R.M., Allen S.W., Fabian A.C., 2001, ApJ, 550, L19
- Dupke R.A., White III R.E., 2000, ApJ, 528, 139
- Edge A.C., Stewart G.C., 1991, MNRAS, 252, 414
- Ettori S., Fabian A.C., Allen S.W., Johnstone R.M., 2002, MNRAS, 331, 635
- Fabian A.C., Hu E.M., Cowie L.L., Grindlay J., 1981, ApJ, 248, 47
- Fabian A.C., Nulsen P.E.J., Canizares C.R., 1984, Nature, 310, 733
- Fabian A.C., 1994, A&AR, 32, 277
- Fabian A.C. et al., 2000, MNRAS, 318, L65
- Fabian A.C., Sanders J.S., Ettori S., Taylor G., Allen S.W., Crawford C.S., Iwasawa K., Johnstone R.M., 2001a, MNRAS, 321, 33L
- Fabian A.C., Mushotzky R.F., Nulsen P.E.J., Peterson J.R., 2001b, MNRAS, 321, L20
- Fabian A.C., Allen S.W., Crawford C.S., Johnstone R.M., Morris G.M., Sanders J.S., Schmidt R.W., 2002, MNRAS, 332, L50
- Ge J., Owen F.N., 1994, AJ, 108, 1523

- Giovannini G., Cotton W.D, Feretti L., Lara L., Venturi T., 1998, *ApJ*, 493, 632
- Kaastra J.S., Mewe R., 1993, *Legacy*, 3, 16
- Kaastra J.S., Ferrigno C., Tamura T., Paerels F.B.S., Peterson J.R., Mittaz J.P.D., 2001, *A&A*, 365, L99
- Kelson D.D., Zabludoff A.I., Williams K.A., Trager, S.C., Mulchaey, J.S., Bolte M., 2002, *ApJ*, in press.
- Liedahl D.A., Osterheld A.L., Goldstein W.H., 1995, *ApJ*, 438, L115
- McNamara B.R. et al., 2000, *ApJ*, 534, L135
- Moore B., Governato F., Quinn T., Stadel J., Lake G., 1998, *ApJ*, 499, L5
- Navarro J.F., Frenk C.S., White S.D.M., 1997, *ApJ*, 490, 493 (NFW)
- Owen F.N., Eilek J.A, 1998, *ApJ*, 493, 73
- Peres C.B., Fabian A.C., Edge A.C., Allen S.W., Johnstone R.M., White D.A., 1998, *MNRAS*, 298, 416
- Peterson J.R. et al., 2001, *A&A*, 365, L104
- Protassov R., van Dyk D.A., Connors A., Kashyap V.L., Siemiginowska A., 2002, *ApJ*, 571, 545
- Sanders J.S., Fabian A.C., 2001, *MNRAS*, 325, 178
- Sanders J.S., Fabian A.C., 2002, *MNRAS*, 331, 273.
- Schmidt R.W., Allen S.W, Fabian A.C., 2001, *MNRAS*, 328, 37
- Tamura T. et al., 2001, *A&A*, 365, L87

This paper has been typeset from a $\text{\TeX}/\text{\LaTeX}$ file prepared by the author.